GRANULAR SEGREGATION IN COLLISIONAL SHEARING FLOWS

Michel Y. Louge, James T. Jenkins, Haitao Xu, and Birgir Ö. Arnarson
Cornell University, Ithaca, New York, USA
MYL3@cornell.edu

Abstract This paper considers segregation in collisional granular shearing flows from the experimental, computational, and theoretical standpoints. We focus on a phenomenon of segregation where the separation of grains by size or mass is driven by spatial gradients in the fluctuation energy of the grains.

We report experiments carried out in microgravity with a shear cell shaped as a race track and containing a mixture of two types of spherical grains. In those experiments, a gradient of fluctuation energy was produced between an inner moving boundary driving collisions among the grains and an outer, more dissipative boundary at the periphery of the cell. The grain segregation and the velocity statistics were captured by a rapid video camera and analyzed using computer-vision software.

We briefly outline a kinetic theory and simulations for these flows. We compare the corresponding profiles of granular concentration, mean velocity, and fluctuation energy with the experimental results.

1. INTRODUCTION

The size segregation of flowing or shaken grains is a commonly observed phenomenon in industrial processes and in nature. In a gravitational field, flows are generally dense and dominated by enduring contacts; their segregation mechanisms are diverse and complex (Savage and Lun 1988, Haff and Werner 1986, Rosato et al. 1986, 1987). In reduced gravity, collisional flows become possible and the segregation is driven mainly by spatial gradients in the energy of granular velocity fluctuations. In steady, fully-developed flows, the balance of momentum exchanged in collisional interaction among different species of grains requires that gradients of particle fluctuation energy be balanced by concentration gradients, thus giving rise to segregation (Jenkins and Mancini 1989).

To observe collisional segregation driven by a fluctuation energy gradient in the direction perpendicular to the flow, we constructed a shear cell in the form of a race track in which the segregation of a sheared binary mixture of two different types of sphere is maintained by the motion of the inner boundary. We conducted experiments on NASA's KC-135 microgravity aircraft. To analyze the resulting images, we developed appropriate vision software. We then compared the profiles of volume fraction and mean and fluctuation velocities with computer simulations of the apparatus. The link between the computer simulations and the physical experiments was achieved by measuring the parameters that characterize individual impacts (Foerster et al. 1994).

To interpret the results of the simulations and experiments, we solved equations governing the spatial variation of the mixture fluctuation energy and velocity. For simplicity, we employed the approximate treatment for the mixture segregation and the transport coefficients of Arnarson and Jenkins (2000), and carried out the averaging of Jenkins and Arnarson (2000) to capture the effects of side walls.

We begin with a brief outline of the theory. Then, we summarize the principle of the simulations, describe the experiments, compare the results, and discuss their significance.

2. SKETCH OF THE THEORY

Because physical experiments inevitably involve boundaries, their interpretation must be conducted with a theory involving these. We briefly outline such a theory for a steady, fully-developed, rectilinear, unidirectional flow in a rectangular cross section bounded by two bumpy boundaries and two flat, frictional walls.

In the absence of an interstitial gas, the steady, fully-developed momentum balance in the flow direction is

$$0 = \frac{\partial \tau_{xy}}{\partial y} + \frac{\partial \tau_{xz}}{\partial z} \,, \tag{1}$$

where τ_{ij} is the granular stress tensor.

The directions x, y, and z are shown in Fig. 1. The origin is located midway between the flat side walls at an ordinate $(d + r_{AB})/2$ above the centers of the stationary boundary bumps, where r_{AB} is the sum of the two species radii and d is the bump diameter. Because the kinetic theory follows the center of interior spheres, its domain occupies a narrower range than the physical experiment, namely $0 \leq y \leq Y'$ and $-Z'/2 \leq z \leq Z'/2$. With bumps of uniform size, $Y' \equiv Y - d - r_{AB}$ and $Z' \equiv Z - r_{AB}$.

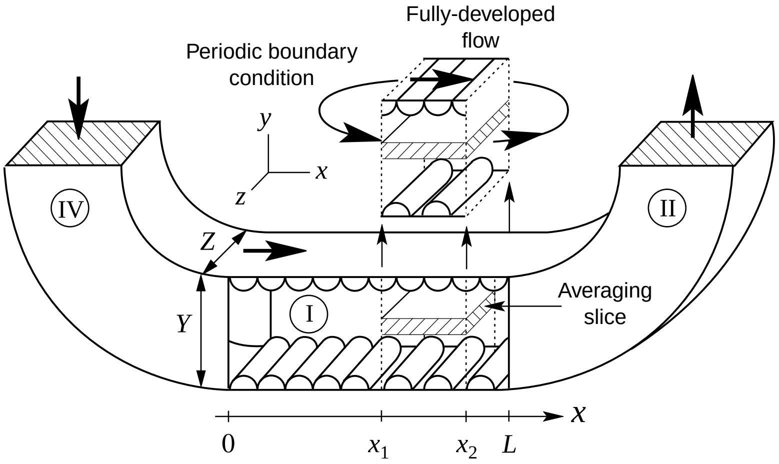

Figure 1 Sketch of the bottom half of the cell. Its straight section (I) has length L, width Y between centers of cylindrical boundary bumps and depth Z between the two flat side walls. Bumps are affixed to both boundaries, including the curved regions (II) and (IV). The upper straight section (III) and the other halves of regions (II) and (IV) are omitted for clarity. Fully developed flows are simulated using a periodic boundary condition in the observation region with $x_1 \le x \le x_2$. Dimensions are not to scale.

The equation governing spatial variations of the mixture fluctuation energy is

$$0 = -\frac{\partial q_y}{\partial y} - \frac{\partial q_z}{\partial z} + \tau_{xy}\frac{\partial u}{\partial y} + \tau_{xz}\frac{\partial u}{\partial z} - \gamma\,, \tag{2}$$

where γ is the volumetric rate of collisional dissipation and q_i is the energy flux. The mixture velocity u along the flow is given by

$$u \equiv \frac{\rho_A\nu_A u_A + \rho_B\nu_B u_B}{\rho_A\nu_A + \rho_B\nu_B}\,, \tag{3}$$

where ρ_α, ν_α, and u_α are the material density, volume fraction, and mean velocity of species α, respectively. Similarly, the mixture temperature T is given by

$$T \equiv \frac{n_A T_A + n_B T_B}{n}\,, \tag{4}$$

where T_α is (2/3) the average fluctuation kinetic energy of species α (Jenkins and Mancini 1989), $n_\alpha = \nu_\alpha\rho_\alpha/m_\alpha$ is its number density, m_α is its mass, and $n = n_A + n_B$.

The shear stress is related to the velocity gradient through the viscosity μ. In fully-developed flow,

$$\tau_{xy} = \mu\frac{\partial u}{\partial y} \quad \text{and} \quad \tau_{xz} = \mu\frac{\partial u}{\partial z}\,. \tag{5}$$

Similarly, the flux is given by

$$q_i = -\kappa \frac{\partial T}{\partial x_i}\,, \tag{6}$$

where κ is the coefficient of thermal conduction. In this work, we adopt the simplified forms of the transport coefficients calculated by Arnarson and Jenkins (2000) for slight differences $\delta r \equiv r_A/r_B - 1$ and $\delta m \equiv (m_A - m_B)/(m_A + m_B)$ in the radii and masses of the two species,

$$\mu = \frac{4}{5}\sqrt{\frac{2}{\pi}}\, n\, r_{AB}\sqrt{m_{AB}T}G(\nu)J(\nu)[1 + (\bar{f}_A - \tfrac{1}{2})(\delta r + \delta m)]\,, \tag{7}$$

and

$$\kappa = 4\sqrt{\frac{2}{\pi}}\, n\, r_{AB}\sqrt{\frac{T}{m_{AB}}}G(\nu)M(\nu)[1 + (\bar{f}_A - \tfrac{1}{2})(\delta r - \delta m)]\,, \tag{8}$$

where n is the mixture number density, m_{AB} is the sum of masses, and G, J, and M are functions of the mixture volume fraction ν:

$$G(\nu) \equiv \frac{\nu(2-\nu)}{2(1-\nu)^3}\,, \tag{9}$$

$$J(\nu) \equiv 1 + \frac{\pi}{12}\left[1 + \frac{5}{8G(\nu)}\right]^2\,, \tag{10}$$

$$M(\nu) \equiv 1 + \frac{9\pi}{32}\left[1 + \frac{5}{12G(\nu)}\right]^2\,. \tag{11}$$

In Eqns. (7) and (8), f_A is the number fraction of species A and the overbar denotes its average value in the cross section. For nearly elastic spheres, the rate of dissipation per unit volume is

$$\gamma \equiv 24\sqrt{\frac{2}{\pi}}\frac{n\,T^{3/2}}{r_{AB}\sqrt{m_{AB}}}G(\nu)(1 - e_{\text{eff}})[1 - (\bar{f}_A - \tfrac{1}{2})(\delta r + \delta m)]\,, \tag{12}$$

where, following Zhang (1993), we incorporate the dissipation due to a modest friction μ_f in collision between grains using an effective restitution coefficient on the order of

$$e_{\text{eff}} \approx e - \frac{\pi}{2}\mu_f\,. \tag{13}$$

Finally, the mixture pressure is

$$P = \frac{24\nu T}{\pi r_{AB}^3}[1 - 3(\bar{f}_A - \tfrac{1}{2})\delta r]\left[1 + \frac{1}{4G(\nu)}\right]G(\nu)\,. \tag{14}$$

Our experience with the simulations is that the flat side walls play a relatively minor role in this flow. Thus, rather than carrying out a numerical integration of Eqns. (1) and (2), we follow Jenkins and Arnarson (2000) by first integrating these along z. For simplicity, we assume that the mixture kinetic energy and species volume fractions are uniform in that direction, that the average along z of the square of the shear stress τ_{xy} is equal to the square of its average, and that the shear stress τ_{xz} is proportional to z and vanishes at the centerline by symmetry. In that case, Eqns. (1) and (2) reduce to

$$\frac{\partial \left<\tau_{xy}\right>}{\partial y} + \frac{2}{Z'}\tau_{xz}^{+} = 0 \tag{15}$$

and

$$-\frac{\partial q_y}{\partial y} + \frac{\left<\tau_{xy}\right>^2}{\mu} - \gamma + \frac{1}{Z'}(q_z^{-} - q_z^{+}) + \frac{1}{3\mu}{\tau_{xz}^{+}}^2 = 0\,, \tag{16}$$

where $\left<\tau_{xy}\right> = \mu\, \mathrm{d}\left<u\right>/\mathrm{d}y$. In these expressions, brackets denote the averaging along z; they are omitted for those variables which, from our assumptions, are constant along that direction. The superscripts + and − represent quantities at the flat side walls at $z = +Z'/2$ and $-Z'/2$, respectively. Jenkins (1992) and Jenkins and Louge (1997) derived expressions for, respectively, the granular stress and the granular flux of fluctuation kinetic energy. If all spheres are sliding at the side wall,

$$\tau_{xz}^{-} = -\tau_{xz}^{+} = \mu_f P \tag{17}$$

and

$$q_z^{-} = -q_z^{+} = b_s P \sqrt{\frac{T}{m_{AB}}}\,, \tag{18}$$

where μ_f is the Coulomb friction coefficient of spheres impacting the walls and b_s is a known function of volume fraction and wall impact parameters. When the spheres roll rather than slide, the stresses and fluxes are functions of the mean relative velocity of the contact point of the grains with the wall, which we evaluate in terms of the mean center of mass velocity assuming that the granular spin equals half the granular vorticity.

At the bumpy boundaries, we employ the conditions derived by Jenkins, Myagchilov, and Xu (2000), who refined the conditions calculated by Richman and Chou (1988) for smooth bumps by adding nonlinear corrections in the slip velocity that remain accurate when the latter becomes large. We incorporate frictional interactions on the bumps in the simple way proposed by Jenkins and Arnarson (2000). Then, the boundary conditions for the temperature are found from a balance of fluctuation energy at the stationary wall,

$$\frac{\mathrm{d}T}{\mathrm{d}y} = -2b_0 \frac{T}{r_{AB}} \, , \tag{19}$$

and at the moving wall,

$$\frac{\mathrm{d}T}{\mathrm{d}y} = +2b_Y \frac{T}{r_{AB}} \, , \tag{20}$$

where b_0 and b_Y are complicated functions of the parameters of impact with the bumps, the stress ratio $\langle \tau_{xy} \rangle / P$, and the wall bumpiness

$$\theta \equiv \sin^{-1} \left(\frac{d+s}{d+r_{AB}} \right) , \tag{21}$$

which is an average measure of the penetration of a sphere of either species in bumps of spacing s between adjacent cylinder edges. Similarly, the velocity boundary conditions are derived from a momentum balance near the stationary boundary,

$$\frac{\mathrm{d}\langle u \rangle}{\mathrm{d}y} = \frac{P}{\mu} \sqrt{\frac{m_{AB}}{\pi T(0)}} f_0 \big(\langle u(0) \rangle \big) \, , \tag{22}$$

and the boundary moving with speed U,

$$\frac{\mathrm{d}\langle u \rangle}{\mathrm{d}y} = \frac{P}{\mu} \sqrt{\frac{m_{AB}}{\pi T(Y)}} f_Y \big(U - \langle u(Y) \rangle \big) \, , \tag{23}$$

where f_0 and f_Y are complicated functions of bump impact parameters, wall bumpiness and relative velocity.

To capture the segregation, we adopt the one-dimensional form of the simplified transport equation for f_A proposed by Arnarson and Jenkins (2000). In the absence of gravity,

$$\frac{\mathrm{d}f_A}{\mathrm{d}y} = -f_A(1-f_A) \frac{1}{T} \frac{\mathrm{d}T}{\mathrm{d}y} \left[R(\nu)\delta r + \Gamma(\nu)\delta m \right] \, , \tag{24}$$

where

$$\Gamma(\nu) \equiv \frac{179}{29} G(\nu) + \frac{105}{116} \, , \tag{25}$$

$$\begin{aligned} R(\nu) \equiv \frac{5}{58} & \left[2 + \frac{\nu(3-\nu)}{2-\nu} - \frac{12}{5} G(\nu) \right] \\ & + 2G(\nu) \left[3 + \frac{\nu(3-\nu)}{2-\nu} \right] - \frac{12\nu H(\nu)[1+4G(\nu)]}{1+4G(\nu)+4\nu H(\nu)} \, , \end{aligned} \tag{26}$$

and

$$H(\nu) \equiv \frac{\mathrm{d}G(\nu)}{\mathrm{d}\nu}\,. \tag{27}$$

Here, we determine lateral profiles of $\langle u \rangle$, T, and f_A by solving Eqns. (15), (16), and (24) numerically subject to conditions (19), (20), (22), and (23), and for given values of the mean volume fraction $\bar{\nu}$ and mean number fraction $\bar{f}_A$.

3. SIMULATIONS

The simulations follow the dynamics of an ensemble of two species of spheres interacting with the boundaries and among themselves through individual impacts. They are based on the algorithm described by Hopkins and Louge (1991). In that algorithm, collisions occur when a sphere overlaps slightly with another sphere or with the wall. The algorithm adjusts its time step periodically to ensure that the mean overlap is kept below a negligible tolerance. In addition, a search grid is superimposed on the flow domain to permit fast identification of near neighbors. Because this method makes it superfluous to maintain a list of future impacts, its computing time is merely proportional to the number of spheres and, consequently, it can simulate the entire shear cell on a relatively small workstation.

Profiles of solid volume fraction, velocity, and temperature for the two grain species are measured by dividing the flow domain into a number of averaging slices (Fig. 1). The average value $\langle \psi \rangle$ of an intrinsic grain property ψ in a slice is calculated by considering a number N_j of instantaneous realizations of the flow, by summing all contributions from N_k spheres passing through the slice over all realizations, and by dividing the result by N_j and N_k. This center-averaging is consistent with the theory outlined earlier. In the absence of gravity, all grain velocities scale with the velocity U of the boundary. In addition, we make the fluctuation energy dimensionless with U^2 and $m_{AB}/2$. Dimensionless quantities are denoted by a dagger ($\dagger$).

Because any rigid boundary tends to order spheres in its neighborhood, the transverse profiles of solid volume fraction exhibit spatial oscillations near the bumpy inner and outer walls with wavelength on the order of a sphere diameter. Because the kinetic theory ignores these fluctuations, their presence can hinder comparisons of the measured segregation with the corresponding theoretical predictions. In grain mixtures, we alleviate this difficulty by focusing on the relative number fraction ϕ rather than the volume fractions of each individual species. For example, for species A,

$$\phi_A \equiv \frac{f_A}{\bar{f}_A} = \frac{(r_B/r_A)^3 + \bar{\nu}_B/\bar{\nu}_A}{(r_B/r_A)^3 + \nu_B/\nu_A}\,. \tag{28}$$

Values of ϕ_A above unity indicate a local surplus of species A spheres. As long as the radii of the two species are not greatly different, the relative number fractions incorporate ratios of volume fractions that nearly oscillate in phase and, consequently, their own spatial fluctuations are considerably reduced.

In the simulations, impacts are characterized in terms of three coefficients (Walton 1988). The first is the coefficient of normal restitution e. The second is the coefficient of friction μ_f for sliding impacts. The last is the coefficient of tangential restitution β_0 for impacts that do not involve sliding. For collisions between two free spheres or between a sphere and one of the flat side walls, we measured these parameters with the facility described by Foerster et al. (1994); for collisions with a cylindrical boundary bump, we adopted the method of Lorenz et al. (1997). Table 1 summarizes the impact parameters.

Table 1 Impact properties

Sphere 1	r_1 (mm)	ρ_1 (g/cm^3)	Sphere 2, bump or wall	r_2 (mm)	ρ_2 (g/cm^3)	e	μ_f	β_0
Acrylic	1.6/1.98	1.22	Acrylic	1.6/1.98	1.22	0.93	0.12	0.35
Ceramic	1.59	3.86	Ceramic	1.59	3.86	0.97	0.10	0.24
Acrylic	1.6/1.98	1.22	Ceramic	1.59	3.86	0.93	0.11	0.10
Acrylic	1.6/1.98	1.22	Fixed bump	1.59	—	0.97	0.22	0.28
Ceramic	1.59	3.86	Fixed bump	1.59	—	0.68	0.08	0.29
Acrylic	1.6/1.98	1.22	Aluminum	∞	—	0.94	0.14	0.51
Ceramic	1.59	3.86	Aluminum	∞	—	0.61	0.10	0.14
Acrylic	1.6/1.98	1.22	Glass	∞	—	0.83	0.12	0.34
Ceramic	1.59	3.86	Glass	∞	—	0.96	0.09	0.00

4. EXPERIMENTS

The apparatus is shaped as a race track. Its straight sections have dimensions $L = 419$ mm, $Y = 29$ mm and $Z = 40$ mm; they permit granular segregation in a rectilinear shearing flow without significant body forces. The grains are recycled through circular regions of a similar cross section and an inner radius of 62 mm. The moving boundary consists of a chain to which closely spaced hemi-cylindrical stainless steel rods with $d = 3.2$ mm are affixed. The chain is driven by a direct-current motor connected to one of the sprockets through a timing belt.

The surface of the outer stationary boundary is made bumpy with similar hemi-cylinders. In the curved regions, these cylinders are closely spaced ($s = 0$). In the upstream half of the straight regions, the separation gradually increases to $s = 1.6\,\mathrm{mm}$, and it remains at this value in the downstream half where observations were carried out. The texture of the stationary boundary is meant to maintain the grains as agitated as possible in the curved sections, while providing a smooth transition to a steep temperature profile in the neighborhood of the observation window.

Flat side walls provide lateral containment and allow the flow to be viewed through glass windows. A digital Kodak EktaPro R0 camera images a 25 mm wide region of the cell with abscissa from the upstream sprocket axis in the range $x_1 \leq x \leq x_2$, where $x_1 = 292\,\mathrm{mm}$ and $x_2 = 326\,\mathrm{mm}$. The spheres exhibit excellent sphericity and narrow size distribution. Their finish allows the vision software to track their movement with accuracy. Louge et al. (2000) describe the computer image analysis. A typical image is shown in Fig. 2. As long as the displacement between two consecutive frames remains less than a sphere radius, this method permits unambiguous tracking of the moving spheres. Adequate lighting is an important condition for success of the computer vision. The field of view is illuminated with two optical-fiber light guides. The shutter speed of the camera, the opening of the lens, and the illumination level are tuned by trial and error until grains are reliably detected.

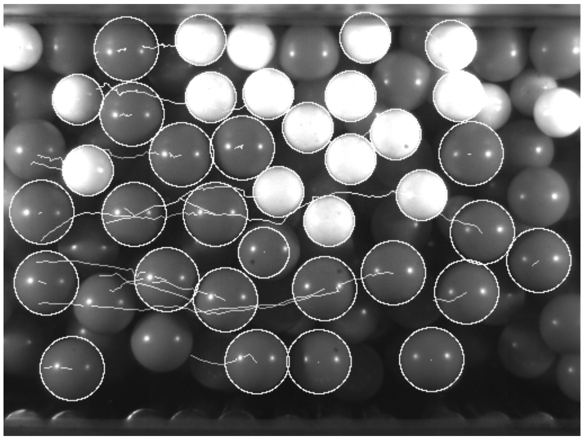

Figure 2 A typical image for the conditions of Test I. Circles and lines are superimposed to indicate the location and trajectory of detected spheres. The moving boundary can be discerned at the bottom of the picture.

Table 2 Experimental conditions

Test	U (m/s)	F (Hz)	Species A	r_A (mm)	$\bar{\nu}_A$ %	Species B	r_B (mm)	$\bar{\nu}_B$ %	$t^\dagger$	t_0 (s)
I	1.4	1000	Ceramic	1.59	10	Acrylic	1.98	30	300	10
II	0.9	500	Acrylic	1.6	28	Acrylic	1.98	5	250	10

The vision algorithm typically detects grains located within a sphere diameter from the window. The two species are then distinguished according to their distinct gray scale or size. Each frame is subdivided into ten horizontal strips of constant width spanning the entire length of the image. By incrementing the observed sphere cross-sectional area intersecting each strip, the vision algorithm calculates the fraction of the strip surface occupied by each species within the field of view and estimates the corresponding relative number fraction by substituting this fraction for ν in Eqn. (28). The simulations showed that transverse profiles of ϕ produced by this method closely represent the state of segregation in the interior. Sphere velocities are then calculated from the positions of each sphere center in two consecutive images and the corresponding center-averaging statistics are incremented as in the simulations. They are made dimensionless with the chain speed directly measured from the image sequence.

Table 2 summarizes experimental conditions for the flight tests in the KC-135 microgravity aircraft. A typical KC-135 trajectory included a gravitational pull of order $18\,\mathrm{m/s^2}$ followed by a parabolic flight yielding 20 s of reduced gravity. We began each test by starting the motor at the onset of the parabola. Peak-to-peak gravity fluctuations remained typically below $\pm\,0.1\,\mathrm{m/s^2}$. The simulations helped us prescribe mixtures for which these fluctuations had minimal effects on the flow, and provided estimates of the dimensionless time $t^\dagger = tU/Y$ required for each experiment to re-establish steady segregation after canceling that level of residual acceleration. Based on those estimates, we waited a time t_0 after the onset of reduced gravity to acquire images with the camera.

Electrostatic charging of the dielectric flow spheres was mitigated by maintaining high relative humidity in the apparatus. With this precaution, no evidence of such charging could be observed.

5. RESULTS AND DISCUSSION

The opacity of the grain assembly and the flow development in the straight section make it challenging to compare experiments and theory directly. While the latter predicts average quantities in the interior of a fully-developed flow, the former observe these quantities through side walls in a developing flow. Although flow variables vary little in the z direction, thus making lateral observations representative of the state in the interior, the flow development remains a more serious impediment to direct comparisons between experiments and theory (Fig. 3).

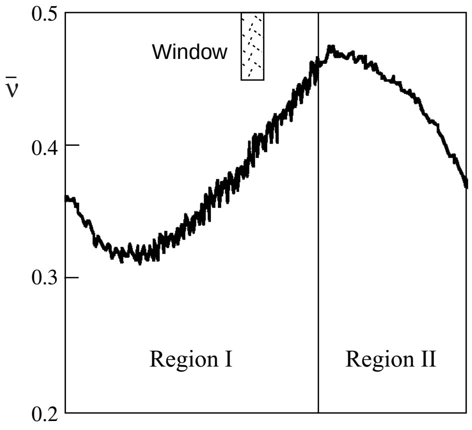

Figure 3 Development of the cross-sectional averaged solid volume fraction along the cell for the conditions of Test I.

In contrast, the simulations can be matched separately with experiments or theory. For comparisons with experiments, we simulate the flow in the entire cell while reproducing the method of imaging, as follows. Because the vision software detects spheres within a depth of focus on the order of r_{AB}, the simulations calculate observable quantities only from spheres centered within that distance from the window. To evaluate the corresponding statistics, the simulations ignore their knowledge of sphere velocities. Instead, they collect the locations (x, y) of visible sphere centers from virtual images generated at the frame rate of the camera. From these, they infer two components of the center velocity and proceed to calculate strip statistics in the same manner as in the experiments.

As Figs. 4 and 5 illustrate with Test II, the simulations reproduce well the fluctuation velocities and segregation observed in the experiments. Louge et al. (2000) reported similar results with Test I. This agreement demonstrates the utility of the simulations as an equal partner to theory and physical experiment. In this event, fewer physical experiments need be done, and the simulations can be used to evaluate the accuracy of the theoretical modeling.

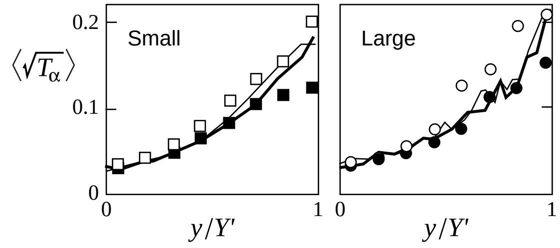

Figure 4 Transverse profiles of the dimensionless fluctuation velocities for the conditions of Test II. The symbols and lines are experimental measurements and predictions of the simulations, respectively. The open symbols and thin lines refer to the x direction, while the closed symbols and thick lines refer to the y direction. The squares and circles represent small and large acrylic spheres, respectively.

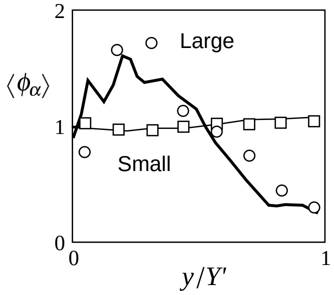

Figure 5 Transverse profiles of the relative number fraction for the conditions of Test II. For symbols and lines, see Fig. 4.

Such an evaluation is shown in Fig. 6. Here, after simulating the entire cell, we extracted an observation region in the range $x_1 \leq x \leq x_2$, to which we imposed the periodic boundary condition sketched in Fig. 1. The spheres contained in this region thus experienced a fully developed flow, which could be matched with results of the theory. Note that, because the periodic simulations were carried out with an actual sample of the developing flow, their species volume fractions were not necessarily equal to those in the entire cell.

As this figure illustrates, the theory captures segregation better at low solid volume fraction. Our conjecture is that higher particle number densities introduce geometric obstacles that the continuum kinetic theory ignores.

Acknowledgments

This research was sponsored by NASA's Microgravity Science and Applications Division under contracts NCC3-468 and NAG3-2112.

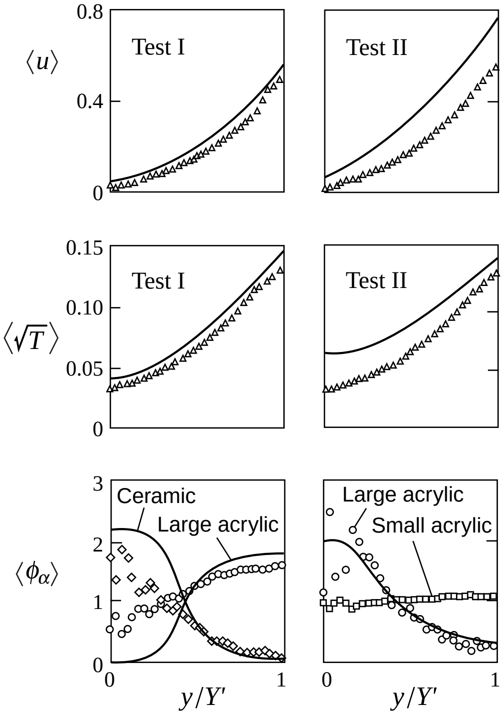

Figure 6 Transverse profiles of dimensionless mixture mean velocity, mixture fluctuation velocity, and relative number fraction for the conditions of Test I (left) and II (right). Triangles and lines represent simulations and theoretical predictions, respectively. In the bottom graphs, circles, diamonds, and squares are simulations results for large acrylic, ceramic, and small acrylic spheres, respectively. In these fully-developed flows, Test I has volume fractions $\bar{\nu}_A = 12.0\%$ and $\bar{\nu}_B = 27.5\%$, and Test II has $\bar{\nu}_A = 25.0\%$ and $\bar{\nu}_B = 4.3\%$.

The authors are indebted to Anthony Reeves for designing the computer vision algorithm and for producing the corresponding velocity statistics; to Gregory Aloe, Roshanak Hakimzadeh, Jeffrey Larko, and Elaina McCartney for participating in the KC-135 flights; and to the engineering team at the NASA–Glenn Research Center: Joe Balombin, Christopher Gallo, Frank Gati, Roshanak Hakimzadeh, Jeffrey Larko, Pamela Mellor, Emily Nelson, Enrique Ramé, Leon Rasberry, John Yaniec and Gary Wroten; and to the KC-135 flight crews and ground support team.

References

Arnarson, B. Ö., and J. T. Jenkins. 2000. Binary mixtures of inelastic spheres: simplified constitutive theory. In preparation.

Foerster, S., M. Y. Louge, H. Chang, and K. Allia. 1994. Measurements of the collision properties of small spheres. *Physics of Fluids* **6**, 1108–1115.

Haff, P. K., and B. T. Werner. 1986. Computer simulation of the mechanical sorting of grains. *Powder Technology* **48**, 239–245.

Hopkins, M. A., and M. Y. Louge. 1991. Inelastic microstructure in rapid granular flows of smooth disks. *Physics of Fluids A* **3**, 47–57.

Jenkins, J. T. 1992. Boundary conditions for rapid granular flows: flat, frictional walls. *Journal of Applied Mechanics* **59**, 120–127.

Jenkins, J. T., and B. Ö. Arnarson. 2000. The influence of side walls on a collisional shearing flow. In preparation.

Jenkins, J. T., and M. Louge. 1997. On the flux of fluctuation energy in a collisional grain flow at a flat, frictional wall. *Physics of Fluids* **9**, 2835–2840.

Jenkins, J. T., and F. Mancini. 1989. Kinetic theory for binary mixtures of smooth, nearly elastic spheres. *Physics of Fluids A* **1**, 2050–2057.

Jenkins, J. T., S. V. Myagchilov, and H. Xu. 2000. Nonlinear boundary conditions for collisional grain flows. In preparation.

Lorenz, A., C. Tuozzolo, and M. Y. Louge. 1997. Measurements of impact properties of small, nearly spherical particles. *Experimental Mechanics* **37**, 292–298.

Louge M. Y., J. T. Jenkins, A. Reeves, and S. Keast. 2000. Microgravity segregation in collisional granular shearing flows. In *Segregation in Granular Flows* (A. D. Rosato, ed.). Dortrecht: Kluver Academic Publishers, in press.

Richman, M. W., and C. S. Chou. 1988. Boundary effects on granular shear flows of smooth disks. *Zeitschrift für angewandte Mechanik und Physik* **39**, 885–901.

Rosato, A., K. J. Strandburg, F. Prinz, and R. H. Swendsen. 1986. Monte Carlo simulation of particulate matter segregation. *Powder Technology* **49**, 59–69.

Rosato, A., K. J. Strandburg, F. Prinz, and R. H. Swendsen. 1987. Why the Brazil nuts are on top: Size segregation of particulate matter by shaking. *Physical Review Letters* **58**, 1038–1040.

Savage, S. B., and C. K. K. Lun. 1988. Particle size segregation in inclined chute flow of dry cohesionless granular solids. *Journal of Fluid Mechanics* **189**, 311–335.

Walton, O. R. 1988. Granular solids flow project. Quarterly report, January–March 1988, UCID-20297-88-1, Lawrence Livermore National Laboratory.

Zhang, C. 1993. Kinetic theory for rapid granular flows. Ph.D. thesis, Cornell University.